



Hybrid nanostructured PAN@NiCu(CO₃)(OH)₂ composite for flexible high-performance supercapacitors

Damin Lee^{1,2,a)}, Anjneya Verma¹, Khan Lê¹, Thomas Fischer¹, Kwang Ho Kim^{2,3}, Sanjay Mathur¹

¹Department of Chemistry, Inorganic and Materials Chemistry, Cologne University, 50939 Cologne, Germany

²Global Frontier R&D Center for Hybrid Interface Materials, Pusan National University, San 30 Jangjeon-dong, Geumjeong-gu, Pusan 609-735, Republic of Korea

³School of Materials Science and Engineering, Pusan National University, San 30 Jangjeon-dong, Geumjeong-gu, Pusan 609-735, Republic of Korea

^{a)}Address all correspondence to this author. e-mail: damin91@pusan.ac.kr

Received: 2 June 2021; accepted: 11 August 2021; published online: 22 October 2021

A binder-free porous NiCu(CO₃)(OH)₂ composite was grown on a polyacrylonitrile (PAN) nanofiber substrate using a hydrothermal method. PAN nanofibers were fabricated by the electrospinning method, thus producing a substrate with a nano-sized diameter and high specific surface area. The composite NiCu(CO₃)(OH)₂ nanowires on PAN nanofibers provided the large specific surface area required for the redox reaction. Transition metal-based nanowires and nano-sized PAN substrates indicate a synergistic effect in electrochemical performance. The NiCu(CO₃)(OH)₂ on PAN composite showed a remarkable maximum specific capacity of 870 mAh g⁻¹ at a current density of 3 A g⁻¹, which indicates that it can be a suitable electrode material. In addition, an asymmetric supercapacitor with NiCu(CO₃)(OH)₂ on PAN composite as the cathode and graphene as the anode showed an ultra-high energy density of 89.2 W h kg⁻¹ at a power density of 835 W kg⁻¹ and a capacitance retention of 90.1% after 5000 cycles.



Damin Lee

Damin Lee received her PhD in 2020 from the Department of Materials Science and Engineering at Pusan National University, Korea. Her PhD thesis was focused on the synthesis and electrochemical properties of transition metal carbonate-hydroxide electrode materials for high-performance supercapacitors. Currently, she is working in Prof. Sanjay Mathur's group as a postdoctoral researcher at Institute of Inorganic Chemistry, University of Cologne, Germany. She was earlier a researcher at Global Frontier R&D Center for Hybrid Interface Materials at Pusan National University. She continues to investigate the fabrication and characterization of supercapacitor devices based on polymers and transition metals composites.

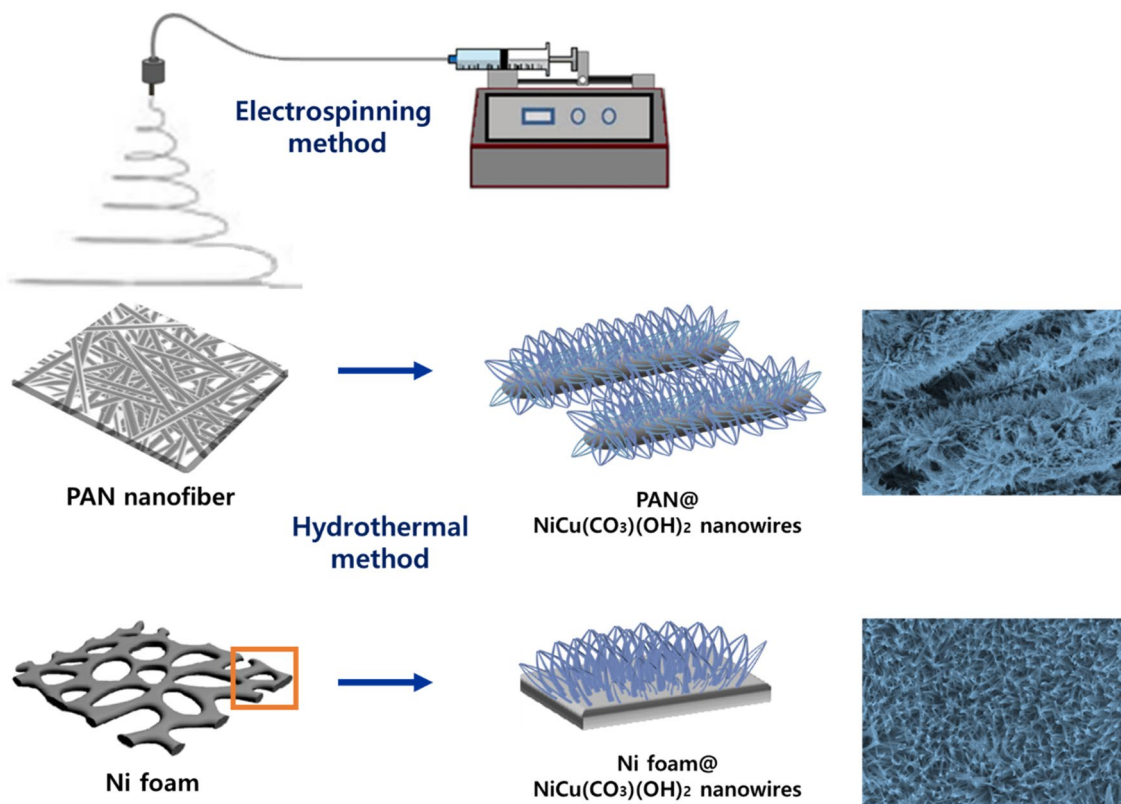
Introduction

In recent years, energy consumption has increased worldwide as human well-being has become increasingly reliant on digital tools, and consequently, the need for high-performance energy storage systems has become prominent [1, 2]. The application of decentralized energy resources and storage technologies in the field of portable, flexible, and smart electronics has significant

challenges that need to be addressed in the global context of energy transition [3, 4]. In this regard, flexible energy devices such as batteries and supercapacitors are key technologies for powering body-worn consumer electronics, sensors, or low-energy bioelectronics (e.g., on-skin diagnostics). Similarly, supercapacitors (SCs) that can fit into various device structures and installation spaces are key enablers for buffering excess

energy. SCs have gained increasing attention owing to their fast charge and discharge rates, high power density, long cycle life, and high reliability [5–7]. However, endowing conventional SCs with good flexibility as well as high energy density is challenging because both charge collectors (substrates) and electrode materials can experience fracture and delamination during flexing. These supercapacitors can be classified into two types: electrical double-layer capacitors (EDLCs), which usually use carbon active materials, and faradaic capacitors, which use redox-active materials [8]. EDLC devices store electrochemical energy via electrostatic accumulation of charges in the electric double layer and currently dominate the SC market because of their ability to accumulate large amounts of charge [9]. However, their relatively low specific capacitance is inhibitive for the increasing requirements of SCs with higher electrochemical performance, which also restricts their potential large-scale applications [10, 11]. Recently, researchers have focused on exploring faradaic capacitors owing to their high specific capacitance, which is induced by fast reversible redox reactions [12]. Faradaic capacitors generally use a metal oxide/hydroxide as the cathode for efficient redox reaction on the electrode surface, which requires an electrode material with a large specific surface area and good electrochemical activity. Transition metal oxides and

hydroxides [13, 14], such as NiO [15], Ni(OH)₂ [16], Co₃O₄ [17], MnO₂ [18], and RuO₂ [19], and their binary composites have been considered as optimized materials for SCs. The reversible redox reaction in faradaic capacitors occurs on the surface of the electrode, and because the electrical energy is stored on the electrode surface, the storage capacity of faradaic capacitors is significantly influenced by electrode material properties. For this reason, binary NiCu-oxide/hydroxide compounds, which exhibit rich redox reactions due to their multiple oxidation states, have been widely used as faradaic capacitors electrodes. For example, Zhenyuan et al. fabricated NiO/Co₃O₄ ultrathin nanosheets that have a specific capacitance of 1775 F g⁻¹ at 1 A g⁻¹ [20]. Jun et al. fabricated Cu-metal organic frameworks (MOF) electrodes, which showed a specific capacitance of 318 F g⁻¹ at 1 A g⁻¹ in a KOH electrolyte [21]. Heba et al. prepared Ni–Cu binary phosphides, which exhibited a specific capacitance of 1573 F g⁻¹ at 1 A g⁻¹ [22]. However, oxide and hydroxide composites normally suffer from gradually decreasing stability after several charging and discharging cycles [23]. In contrast, nanostructured transition metal hydroxy-carbonates are promising alternatives because in addition to their longer cycling lifetime, they offer better hydrophilic properties when reacting to aqueous electrolytes due to the surface-attached carbonate



Scheme 1: The fabrication of the PAN@NiCu(CO₃)(OH)₂ composites and Ni-foam@NiCu(CO₃)(OH)₂ with SEM images of the as-prepared electrodes morphology.

(CO₃²⁻) groups. CO₃²⁻ ions substantially increase the wettability of the electrode surface and thus can achieve higher capacitive efficiency and electrochemical characteristics than the oxide/hydroxide-based materials [24, 25]. Binary transition metal carbonate hydroxide composite (MM'(CO₃)_x(OH)_y) with the general formula exhibit various oxidation states and hence can undergo numerous redox reactions, resulting in good structural stability, high electron conductivity, and reversible capacity [26]. In addition, faradaic capacitors that store electrical energy on the surface of the electrode require a large specific surface area for the redox reaction. To fabricate an electrode with a larger specific surface area, three-dimensional (3D) Ni foam was directly researched as a substrate for SCs in a previous study [27]. 3D binary composites of porous Ni foams have been widely used as electrodes for supercapacitors because of their good electrical conductivity and large specific surface area [28, 29]. However, this type of electrode is unsuitable for use in wearable devices because it can fracture and delaminate while bending. Typically, carbon-based cloth, fibers, and metal foils are used to make flexible electrode materials that are used in conjunction with various polymers such as PAN and polyacrylamide (PAM) to support flexible substrate shapes [30–32]. The current study is focused on improving the electrochemical performance of composite materials obtained by NiCu(CO₃)(OH)₂ on a PAN nanofiber substrate. As shown in Scheme 1, PAN substrates have a much larger surface area than that of Ni foam observed in scanning electron microscopy images with the same magnification. This area provides sufficient space for the growth of transition metal compounds, and the substrate also possesses flexible properties [33]. PAN substrates with nanosized diameters result in a high specific surface area, which can significantly enhance the electrode/electrolyte contact area, shorten the ion paths, facilitate electrolyte penetration, and improve the ion and electron

diffusion [34]. Thus, they exhibit a high electrochemical capacity because the ions at the electrolyte interface are transported easily [35]. Combining these advantages, NiCu(CO₃)(OH)₂ nanowires on the PAN nanofibers substrate have a large specific surface area and reacts well with an aqueous electrolyte for the positive electrode of an SC. This study focuses on the development of flexible SC electrodes with enhanced electrochemical performance by synthesizing PAN nanomeshes via electrospinning of conductive polymers and modifying their surfaces through the growth of binary metal hydroxy-carbonates. This is the easiest and cheapest method to produce a web of nanofibers, which is helpful for commercial fabrication of faradaic capacitors electrode. As a result, the synergy of crystalline metal hydroxy carbonate grown on PAN nanofiber meshes enabled the resulting electrodes to have excellent electrochemical properties.

In this study, the challenge of improving the energy density of SCs while maintaining their high-power response will be addressed by integrating two concepts: (i) hydrothermal growth of transition metal hydroxy carbonates and (ii) electrospinning of conductive polymers to obtain high surface area, porosity, and flexible properties. Herein, the electrochemical properties of NiCu(CO₃)(OH)₂ on a flexible PAN substrate were compared with those of a previously researched NiCu(CO₃)(OH)₂ electrode on a non-flexible Ni-foam substrate. The NiCu(CO₃)(OH)₂ composite on the flexible PAN substrate with a large surface area represented a significantly high specific capacity of 870 mAh g⁻¹ at a current density of 3 A g⁻¹ and a cycling characteristic of 84.1% retention after 5000 cycles. In contrast, the Ni-foam@NiCu(CO₃)(OH)₂ composite showed a low specific capacity of 759 mAh g⁻¹ at a current density of 3 A g⁻¹. Additionally, an asymmetric supercapacitor (ASC) made of the PAN@NiCu(CO₃)(OH)₂ composite as the cathode and graphene as the anode (PAN@NiCu(CO₃)(OH)₂/graphene ASC) had a good energy density of 90 W h kg⁻¹ at a power density of 835 W kg⁻¹ and a current density of 2 A g⁻¹, which was higher than those of most previously reported transition composite ASCs. Consequently, inorganic polymer nanostructures have been shown to improve cell performance owing to the directed charge carrier transport and high surface-to-volume ratios [36, 37]. This will optimally integrate material and electrochemical properties with new material fabrication technologies and chemical processing.

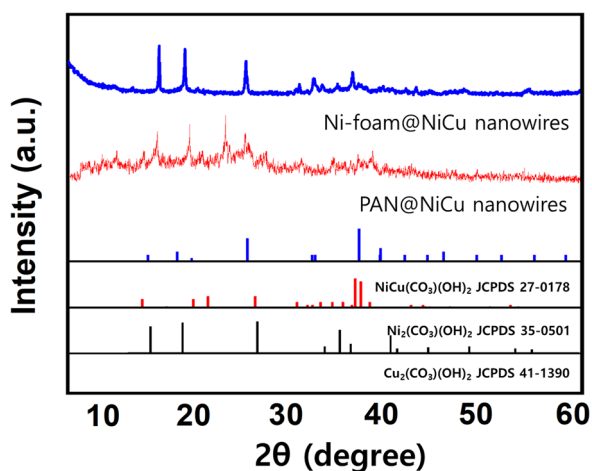


Figure 1: XRD patterns of the Ni-foam@NiCu(CO₃)(OH)₂ and PAN@NiCu(CO₃)(OH)₂ composite electrodes.

Results and discussion

Composition and morphology analysis

The as-synthesized composites of NiCu(CO₃)(OH)₂ on Ni-foam substrate (Ni-foam@NiCu(CO₃)(OH)₂) and PAN substrate (PAN@NiCu(CO₃)(OH)₂) were examined using X-ray diffraction (XRD), X-ray photoelectron spectroscopy (XPS),

scanning electron microscopy (SEM), and Transmission electron microscopy (TEM). The typical XRD patterns of the Ni-foam@NiCu(CO₃)(OH)₂ and PAN@NiCu(CO₃)(OH)₂ composites are shown in Fig. 1. They exhibit characteristic diffraction peaks at 14.8°, 17.5°, 24.1°, and 34.6°, corresponding to the (020), (120), (220), and (201) planes, respectively, which are well-indexed to NiCu(CO₃)(OH)₂ (JCPDS 27-0178) [10]. In addition, the electrodes generally showed peaks for Cu₂(CO₃)(OH)₂ at 14.8° and 17.5°, corresponding to the (020) and (120) planes (JCPDS 41-1390) [38]. All the NiCu(CO₃)(OH)₂ composites showed clear peaks for Ni₂(CO₃)(OH)₂ at 34.7° and 59.8°, corresponding to the (201) and (002) planes, respectively (JCPDS 35-0501) [39]. These results indicate that the electrodes are not a single phase, but a multiphase material. Additionally, the Ni-foam@NiCu(CO₃)(OH)₂ electrode exhibited higher peak intensities than that of the PAN@NiCu(CO₃)(OH)₂ composite, which was fabricated using amorphous PAN as the substrate. In conclusion, the NiCu(CO₃)(OH)₂ electrode fabricated using Ni foam as a substrate exhibited higher crystallinity than that using the PAN substrate. The detailed chemical composition of the as-prepared NiCu(CO₃)(OH)₂ nanowire portion was further evaluated using the XPS technique, which indicates the corresponding results.

The chemical composition of the sample was measured using a powder of the NiCu(CO₃)(OH)₂ nanowire from the electrode with scrapable Ni foam. Figure 2 shows the presence of Ni, Cu, C, and O in the NiCu(CO₃)(OH)₂ nanowire. As shown in Fig. 2a, two spin-orbit coupling peaks at 855.7 and 873.6 eV ascribe to Ni 2p_{3/2} and Ni 2p_{1/2}. And two shake-up satellite peaks (indicated as “sat.”) are identified at 862.2 and 879.7 eV, respectively, which clearly show the presence of Ni²⁺ [40]. In the Cu 2p core spectrum displayed two satellite peaks at 943.4 and 963.5 eV and two peaks for Cu 2p_{3/2} and Cu 2p_{1/2} at 935.2 and 955.8 eV in Fig. 2b, respectively [41]. These peaks confirm the presence of Cu²⁺ in the NiCu(CO₃)(OH)₂ nanowire electrode. The binding energy peaks at 284.8, 285.7, and 289.2 eV could be marked to the typical bands of C–C, C–O, and O–C=O bonds in Fig. 2c, respectively. That represents the presence of metal-carbonate and carbonate groups, indicating the presence of carbonate [42]. Figure 2d indicates the four oxygen species, assigned as O1, O2, O3, and O4. The peak of O1 at 530.2 eV is a typical oxide with copper, and that of O2 at 531.0 eV can be assigned to a hydroxide bond, and that of O3 at 531.6 eV corresponds to C–O (or O–C=O). The O4 peak at 532.8 eV was attributed to the multiplicity of physisorbed and chemisorbed

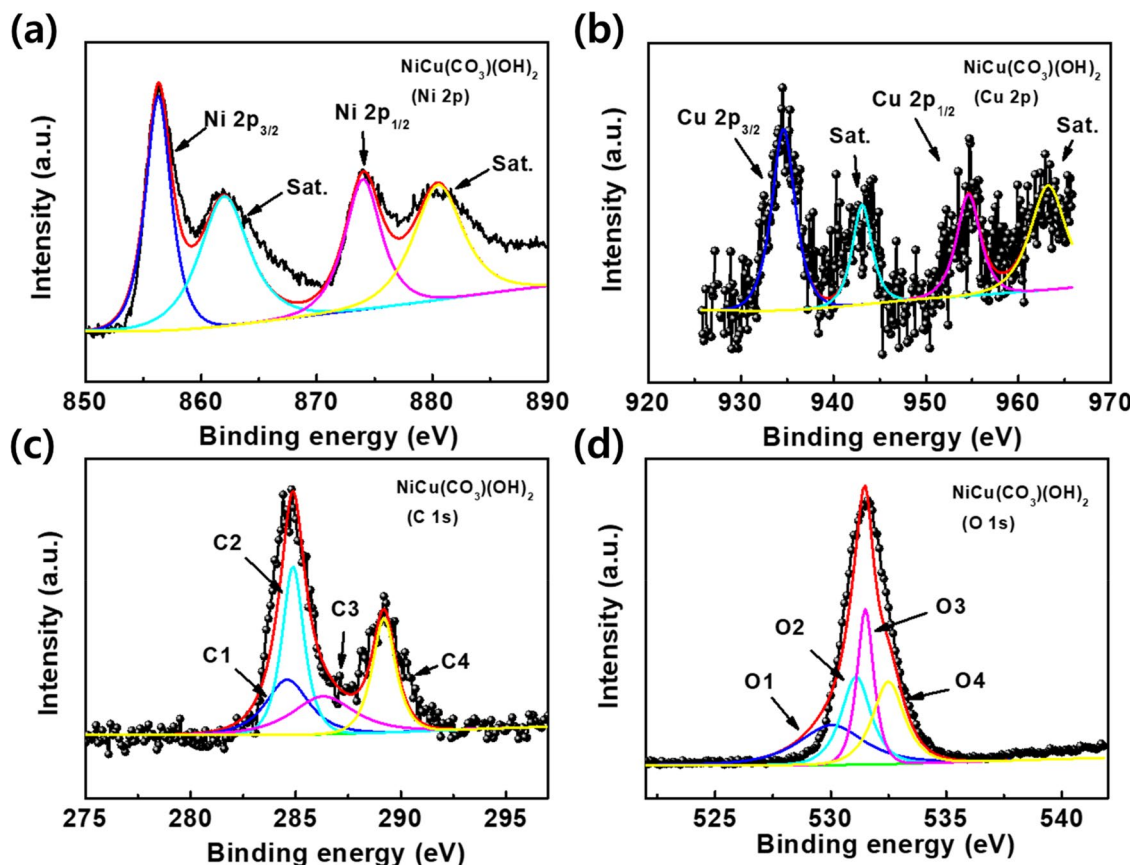


Figure 2: XPS spectra of the NiCu(CO₃)(OH)₂ electrode: (a) Ni 2p, (b) Cu 2p, (c) C 1s, and (d) O 1s.

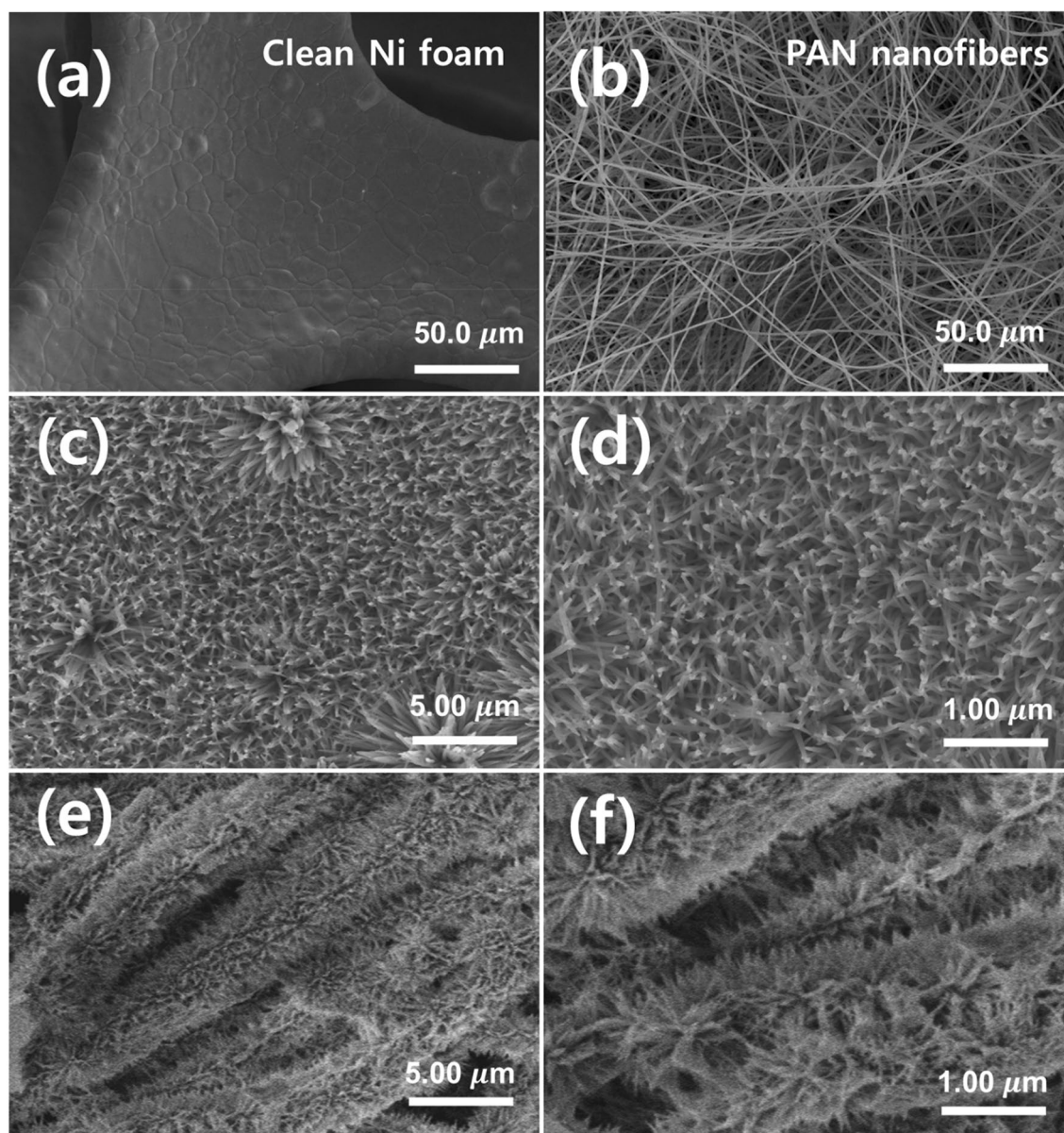


Figure 3: SEM images of (a) the Ni-foam, (b) PAN nanofibers as the substrates at similar magnification; Low- and high-magnification SEM images of (c) and (d) the Ni-foam@NiCu(CO₃)(OH)₂ composite, (e) and (f) the PAN@NiCu(CO₃)(OH)₂ composite.

water at the surface [43]. These XPS results prove that the prepared NiCu(CO₃)(OH)₂ nanowires have composition containing the Ni²⁺, Ni³⁺, Cu²⁺, Cu³⁺, C and O, which can further confirm the composition of NiCu(CO₃)(OH)₂ nanowires electrode. Figure 3 shows the difference between the surface areas of clean Ni foam and PAN nanofibers at similar magnifications. The SEM image of the synthesized PAN nanofiber composite shows a more porous structure than that of the Ni-foam, and the specific surface area on which the NiCu(CO₃)(OH)₂ nanowire can grow is much wider, as shown in Fig. 3b. These results indicate that the PAN nanofiber substrate with a large surface area is a suitable electrode material for the redox reactions of

faradaic capacitors. The NiCu(CO₃)(OH)₂ nanowires on the Ni foam exhibited morphology similar to that of the NiCu(CO₃)(OH)₂ nanowires on the PAN nanofiber. These nanowires were uniformly deposited on the Ni-foam and PAN substrates, which grew freely over the surface without agglomeration, regardless of the substrate type in Fig. 3c–f. Furthermore, the composite grown on the PAN nanofiber has a much larger surface area than that deposited on the Ni foam (Fig. 3c and e). The nanosized PAN fibers and NiCu(CO₃)(OH)₂ composite can provide the large specific surface area required for the redox reaction. As a result, the synergetic effect of NiCu(CO₃)(OH)₂ nanowires and PAN nanofiber substrates with the thin and uniform composite

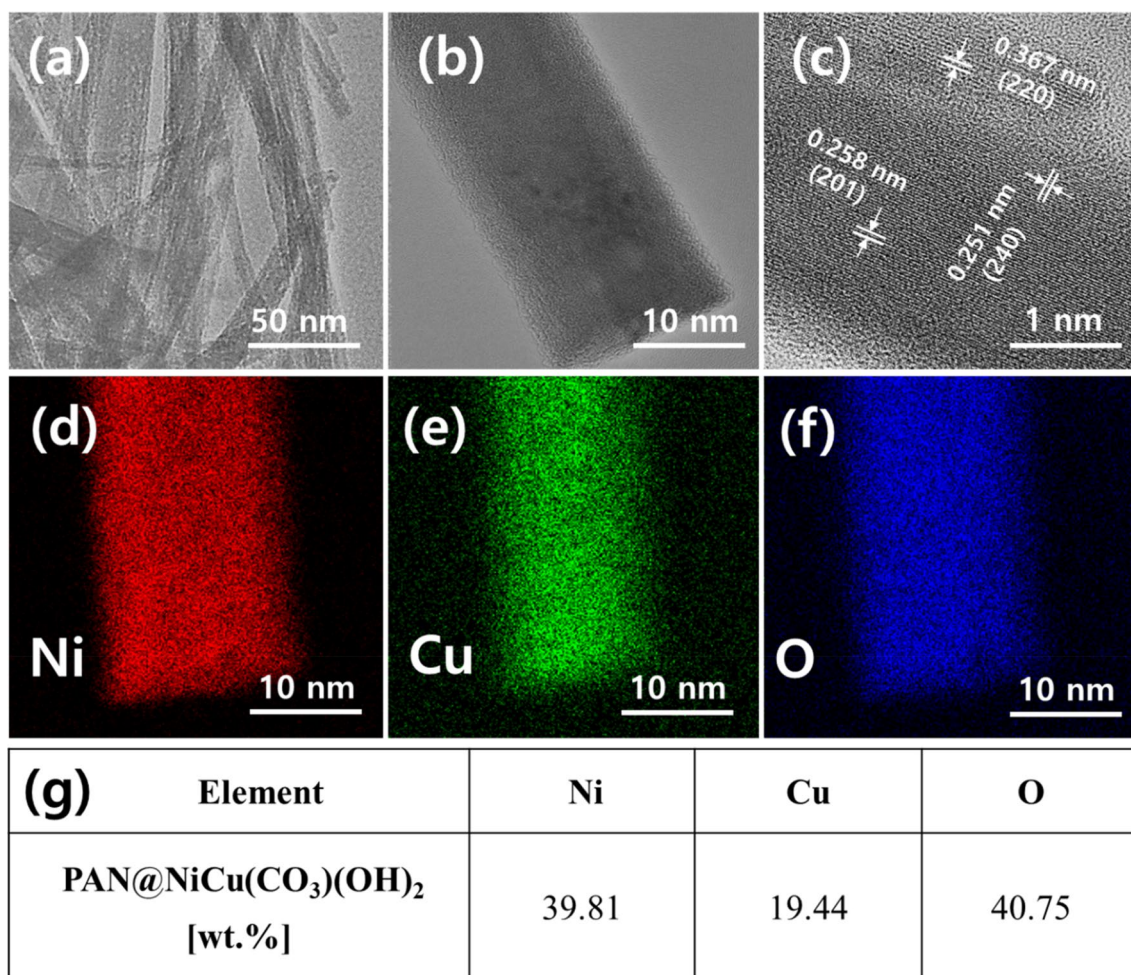


Figure 4: (a and b) Low-magnification TEM images, (c) HR-TEM image of the PAN@NiCu(CO₃)(OH)₂ nanowire composite; elemental mapping of PAN@NiCu(CO₃)(OH)₂ nanowires with color coded contribution of Ni, Cu and O (d-f). (g) Elemental contribution according to EDS mapping in wt% of PAN@NiCu(CO₃)(OH)₂ composite.

provided a remarkably increased electrolyte/electrode contact area and decreased the length of the ion diffusion path. The PAN@NiCu(CO₃)(OH)₂ nanowire electrode increased electron transfer between the layers and enhanced the electrical energy performance of the faradaic capacitors. The microstructures of the PAN@NiCu(CO₃)(OH)₂ nanowires were further researched using TEM. The NiCu(CO₃)(OH)₂ nanowire of the electrode composite was ultrathin and had a stable structure. These nanowires are straight and only a few nanometers thick with a highly porous texture, as shown in Fig. 4. Thus, electrolyte ions are able to diffuse deeply and easily inside the composite and the electrode can achieve high-rate performance. In addition, a defined, continuous heterointerface formed from the fringe could be identified from the nanowires in the high-resolution TEM (HRTEM) image in Fig. 4c. The HRTEM image of the NiCu(CO₃)(OH)₂ composite shows lattice fringes with spacings of 0.251, 0.258, and 0.367 nm, corresponding to the (240), (201), and (220) planes, respectively. These spacings are in agreement

with those of the NiCu(CO₃)(OH)₂ composite [10]. From the morphology of this nanostructure, it can be confirmed that NiCu(CO₃)(OH)₂ nanowires were grown on PAN nanofibers well. Furthermore, to evaluate the surface properties of the PAN@NiCu(CO₃)(OH)₂ nanowire composite, energy-dispersive X-ray spectroscopy (EDS) maps verified the homogeneous composition of the nanofibers by the color-coded elemental distribution corresponding to each ion. Figure 4d-g shows the EDS values for the Ni, Cu, and O contents averaged over the wire area of the PAN@NiCu(CO₃)(OH)₂ composite. Figure 4d-f show the elements of the NiCu(CO₃)(OH)₂ nanowires grown on the PAN nanofibers, respectively. This result confirms that Ni, Cu, and O are uniformly dispersed inside the nanowire structures. When the amount of Cu was half that of Ni, the electrochemical performance of the electrode was optimized. As shown in Fig. 4e, the EDS value of the PAN@NiCu(CO₃)(OH)₂ nanowire composite shows that the weight % of Cu is half that of Ni. The EDS mapping supports the XRD results that the NiCu(CO₃)(OH)₂

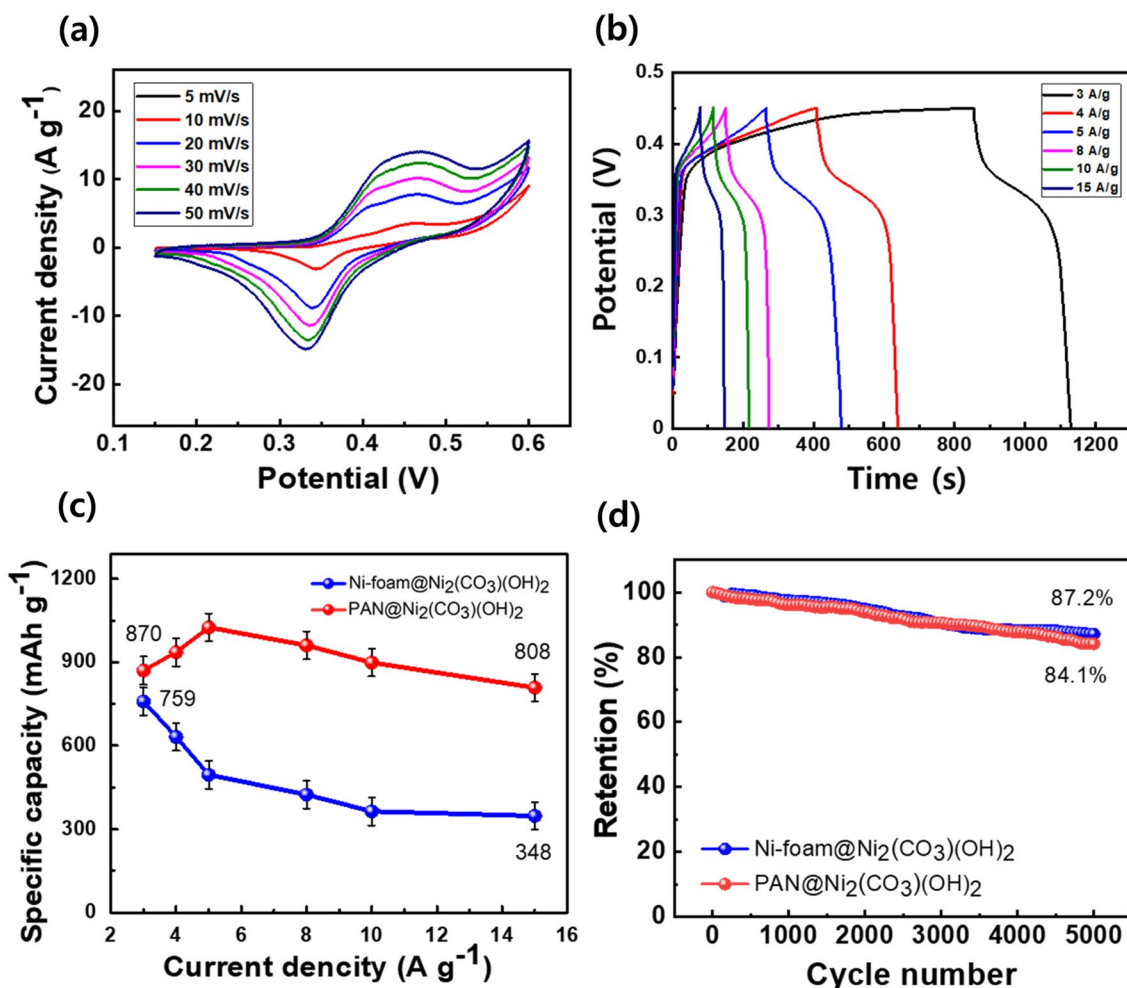


Figure 5: (a) The CV curves, (b) galvanostatic CD curves of the PAN@NiCu(CO₃)(OH)₂ electrode, comparison of (c) the specific capacitance of the NiCu(CO₃)(OH)₂ composite at different current densities, (d) cycling stability of the NiCu(CO₃)(OH)₂ on the Ni-foam and PAN substrates.

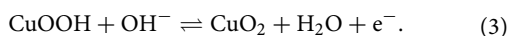
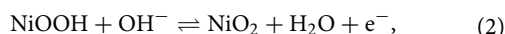
composite with an Ni:Cu ratio of 2:1 formed, which represents the stoichiometric ratio of the educts added to the reaction.

Electrochemical properties

Figure 5a presents the redox curves of the electrodes with a three-electrode cell, which shows the cyclic voltammetry (CV) curves of the PAN@NiCu(CO₃)(OH)₂ composite in the potential window of 0.15–0.6 V at scan rates from 5 to 50 mV⁻¹ in a 1 M KOH electrolyte. The oxidation and reduction peaks in the CV curves shifted toward more positive and negative potentials, respectively, as the scan speed increased because the internal diffusion resistance increased within

the electrode surface. The typical CV peaks of the PAN@NiCu(CO₃)(OH)₂ electrodes showed reduction peak at ~0.46 V, and an oxidation peak at ~0.34 V, respectively, at 10 mV s⁻¹. As the scan rate increased, the redox peak of the PAN@NiCu(CO₃)(OH)₂ electrode shifted to an extent, indicating that there is the internal resistance of the PAN@NiCu(CO₃)(OH)₂ electrode. And the CV of PAN@NiCu(CO₃)(OH)₂ has a large internal area, which is proportional to its capacity value. This result indicates that the PAN@NiCu(CO₃)(OH)₂ electrode has a great electrochemical value. This electrode exhibits symmetric redox peak property, indicating good performance for redox reactions and largely porous morphology. The CV curves obtained for the PAN@NiCu(CO₃)(OH)₂ nanowire electrode were standard for faradaic capacitors. The faradaic redox reactions of the NiCu(CO₃)(OH)₂ composite occurred according to Eqs. (1–3) [44, 45]:





According to these equations, the redox reactions involve OH^- from the electrolyte in the optimized $\text{NiCu}(\text{CO}_3)(\text{OH})_2$ composite. Figure 5b shows the galvanostatic charge–discharge (GCD) measurements of the $\text{PAN@NiCu}(\text{CO}_3)(\text{OH})_2$ composite over a potential range of 0–0.45 V. The GCD curves showed a nonlinear slope and triangular symmetry owing to the occurrence of quasi-reversible redox reactions at the electrolyte/electrode interface. As shown in Fig. 5b, the $\text{PAN@NiCu}(\text{CO}_3)(\text{OH})_2$ composite had a long discharge time, indicating that it has high electrochemical performance, which is consistent with the trend observed in the CV analysis. The specific capacities of the previously tested Ni-foam@ $\text{NiCu}(\text{CO}_3)(\text{OH})_2$ and $\text{PAN@NiCu}(\text{CO}_3)(\text{OH})_2$ composites were calculated using the following Eq. (4) [46]:

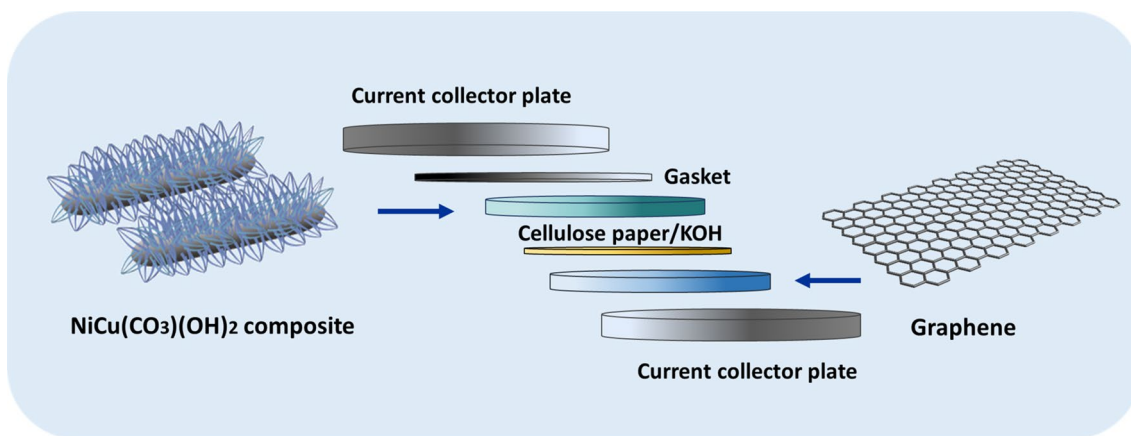
$$Q_D = \frac{I\Delta t}{m} \quad (4)$$

where Q_D (mAh g^{-1}) is the specific capacity, I (mA) is the discharging current, Δt (s) is the discharging time that is measured from 0.0 to 0.45 V, and m (g) is the designated mass of the active material. Using this equation, it was found that the $\text{PAN@NiCu}(\text{CO}_3)(\text{OH})_2$ nanowire composite possessed high electrochemical values. As shown in Fig. 5c, the $\text{PAN@NiCu}(\text{CO}_3)(\text{OH})_2$ electrode exhibited specific capacities of 870, 936, 1025, 960, 899, and 808 mAh g^{-1} , while the specific capacities of the

Ni-foam@ $\text{NiCu}(\text{CO}_3)(\text{OH})_2$ electrode were calculated to be 759, 632, 496, 424, 364, and 348 mAh g^{-1} at current densities of 3, 4, 5, 8, 10, and 15 A g^{-1} , respectively. This was attributed to the positive effect of the increased surface area of the $\text{PAN@NiCu}(\text{CO}_3)(\text{OH})_2$ electrode structure. As a result, $\text{PAN@NiCu}(\text{CO}_3)(\text{OH})_2$ had higher specific capacitance values than the $\text{NiCu}(\text{CO}_3)(\text{OH})_2$ composite on the Ni-foam substrate, which indicates the synergetic effect of the PAN nanofibers and $\text{NiCu}(\text{CO}_3)(\text{OH})_2$ nanowire electrode. The cycling properties were also measured to investigate the stability of the electrodes. Long-term electrical retention is an important factor for electrodes in supercapacitor applications and industrialization [47]. As shown in Fig. 5d, after satisfactory cycles, the Ni-foam@ $\text{NiCu}(\text{CO}_3)(\text{OH})_2$ and $\text{PAN@NiCu}(\text{CO}_3)(\text{OH})_2$ electrodes exhibited retentions of 88.2% and 84.1%, respectively, after 5000 cycles. The stability of the electrodes was evaluated using the discharging time at a constant current density of 10 A g^{-1} . These results suggest that the Ni-foam@ $\text{NiCu}(\text{CO}_3)(\text{OH})_2$ electrode exhibited better cycling stability than the $\text{PAN@NiCu}(\text{CO}_3)(\text{OH})_2$ electrode. The synergistic effects of the PAN substrate and $\text{NiCu}(\text{CO}_3)(\text{OH})_2$ composite contributed to enhanced electrochemical performance for a specific capacitance; however, this electrode possessed a lower retention value owing to its weak polymer properties. Nevertheless, these results indicate better electrochemical properties than those previously reported for NiCu-based electrodes (Table 1). As a result, although the electrode was damaged and the capacity decreased with the increasing number of cycles, it had a high retention value because of the positive influence of the transition metal composites.

TABLE 1: Comparison with the capacitance and retention values of the previously studied nickel- and copper-based electrodes.

Positive electrodes	C (F g^{-1})	Current density	Retention value	Refs.
Ni(OH) ₂ /graphene	1735	1 mV s^{-1}	94.3% (after 3000 cycles)	[48]
Nanospherical NiO	1201	0.5 A g^{-1}	70% (after 500 cycles)	[49]
NiO-3D graphene	1829	3 A g^{-1}	85% (after 5000 cycles)	[50]
NiO/MWCNTs	1727	5 mA cm^{-2}	91% (after 2000 cycles)	[51]
CuO cauliflowers	179	5 mV s^{-1}	81% (after 2000 cycles)	[52]
CuO nanostructure	820	5 mV s^{-1}	90.2% (after 1000 cycles)	[53]
CuO/PANI composite	185	5 A g^{-1}	75% (after 2000 cycles)	[54]
CuO nanosheet	464	5 mV s^{-1}	89% (after 3000 cycles)	[55]
CuCo ₂ O ₄ /CuO nanowire	79	1 A g^{-1}	83% (after 5000 cycles)	[56]
CuCo ₂ O ₄ electrode	1006	1 A g^{-1}	71.2% (after 5000 cycles)	[57]
CuCo ₂ O ₄ nanosheet	1473	1 A g^{-1}	93% (after 5000 cycles)	[58]
CuCo ₂ O ₄ array	1330	2 A g^{-1}	70% (after 5000 cycles)	[59]
NiCu(CO ₃)(OH) ₂ nanowires	971	1 A g^{-1}	91.5% (after 2000 cycles)	[60]
NiCu(OH) ₂ nanoparticle	264.91	1 A g^{-1}	75.8% (after 3000 cycles)	[22]
Ni hexacyanoferrate	294	2 mV s^{-1}	93% (after 2000 cycles)	[61]
NiCu binary oxide	1711	5 A g^{-1}	85% (after 5000 cycles)	[62]
Ni(HCO ₃) ₂ /(Cu _{0.2} Ni _{0.8})O	2000	1 A g^{-1}	75.45% (after 3000 cycles)	[63]
PAN@NiCu(CO ₃)(OH) ₂ electrode	1933	3 A g^{-1}	84.1% (after 5000 cycles)	This work



Scheme 2: Configuration of the NiCu(CO₃)(OH)₂ electrode//graphene ASC device.

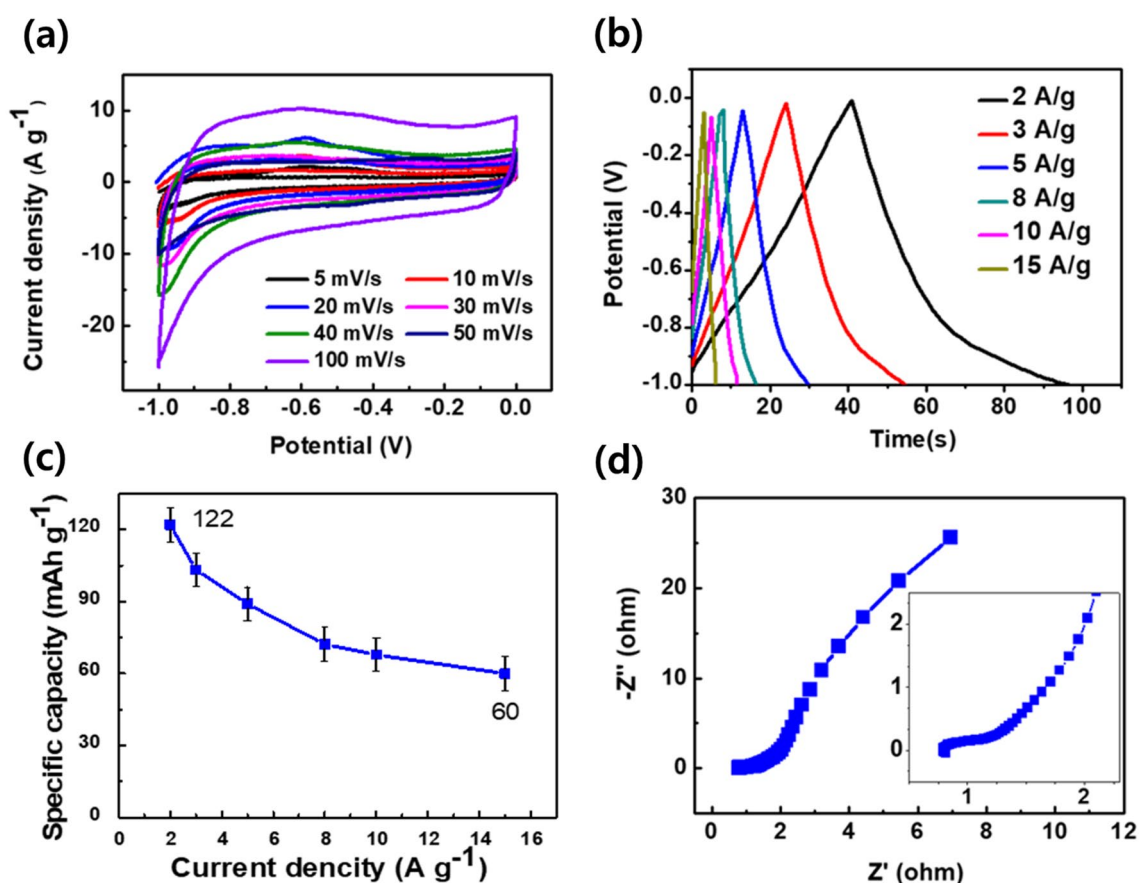


Figure 6: (a) CV curves of the graphene as electrode in negative voltage window at different scan rates, (b) the galvanostatic CD curves of the graphene at different current densities, (c) the specific capacity of the graphene at different current densities, (d) the EIS spectrum of the graphene as electrode.

To further investigate the viability of the electrodes in energy storage devices, an ASC was fabricated using Ni-foam@NiCu(CO₃)(OH)₂ and PAN@NiCu(CO₃)(OH)₂ composites as the cathode and graphene as the anode. A cellulose separator paper and 1 M KOH electrolyte were used for the ASC device.

A schematic diagram of the cathode and anode ASC electrodes is shown in Scheme 2. The electrochemical performance of the graphene electrode was measured in the potential range of -1 to 0 V, as shown in Fig. 6. The CV curves of graphene showed typical rectangular shapes, which represent the ideal

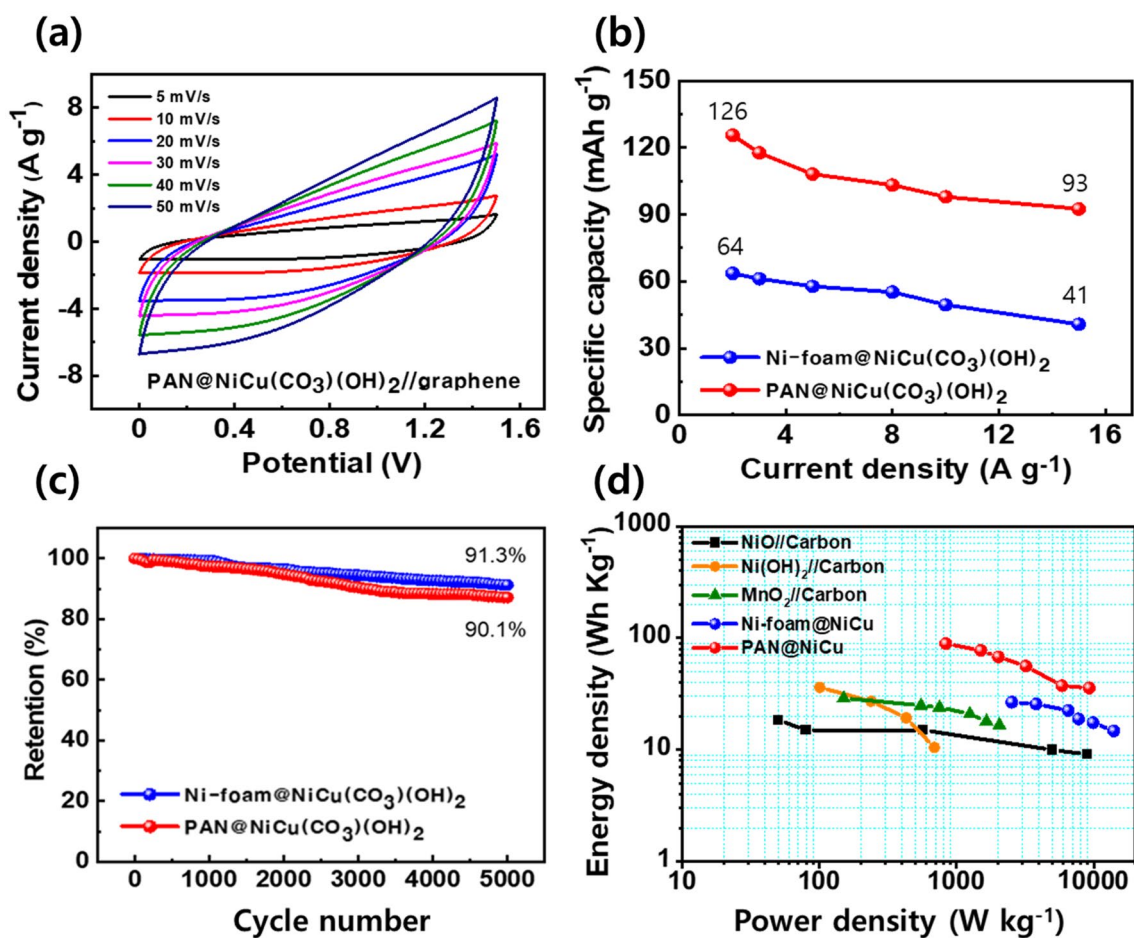


Figure 7: CV curves of (a) the optimized PAN@NiCu(CO₃)(OH)₂//graphene ASC; comparison of (b) the specific capacity, (c) cycling stability of the Ni-foam@NiCu(CO₃)(OH)₂//graphene and PAN@NiCu(CO₃)(OH)₂//graphene ASCs at 5 A g⁻¹, (d) Ragone plot of the ASC devices.

faradaic capacitor (Fig. 6a). The GCD curves exhibited linear and symmetric shapes, as shown in Fig. 6b. The specific capacity (Fig. 6c) of the graphene electrode was 122 mAh g⁻¹ at 2 A g⁻¹ and 60 mAh g⁻¹ at 15 A g⁻¹, respectively. EIS analyses were performed to investigate the conductivity behavior and charge-transfer kinetics of the graphene electrode. In the high-frequency region, the graphene electrode showed low *R_s* and *R_{ct}* values of 0.6 Ω and 0.82 Ω, respectively (inset of Fig. 6d). The slope of the linear section of the graphene electrode has a higher incline in the low-frequency region, which represents a low *Z_w* value, as shown in Fig. 6d. These results confirmed that the graphene electrode could be a suitable negative electrode for ASCs. Figure 7 shows the CV curves of the assembled ASC, which demonstrate electrical double-layer capacitor properties behavior at different scan rates in the voltage range of 0.0–1.5 V. This phenomenon indicates that PAN@NiCu(CO₃)(OH)₂ electrode//graphene ASCs were significantly influenced by graphene, which is a negative electrode material. As shown in Fig. 7a, the PAN@NiCu(CO₃)(OH)₂ composite shows excellent rectangular CV curves, which represent the ideal behavior

of SCs. and this ASC device does not have the redox peaks at all scan rates. Figure 7b represents the specific capacity values of the Ni-foam@NiCu(CO₃)(OH)₂//graphene ASC and PAN@NiCu(CO₃)(OH)₂ electrode//graphene ASC from the discharge times, which are calculated to be 64 mAh g⁻¹ and 126 mAh g⁻¹ at 2 A g⁻¹, respectively. This improvement in electrical performance is achieved by the electrical conductivity of the active materials and electrolyte penetration provided by the PAN nanofiber substrate to undergo a redox reaction. Therefore, high-speed performance is achieved of the development for high-performance faradaic capacitors. The retention values of the ASCs were measured with respect to the discharge time at a current density of 5 A g⁻¹ in Fig. 7c. The assembled ASC of the Ni-foam@NiCu(CO₃)(OH)₂ and PAN@NiCu(CO₃)(OH)₂ electrodes retained 91.3 and 90.1% of their capacities, respectively, after 5000 cycles. The retention values of the ASC were similar after 5000 cycles, regardless of the substrate type. These properties indicate that the PAN@NiCu(CO₃)(OH)₂ electrode can facilitate a more stable cycle reaction when measuring the electrochemical value with the ASC than with the half-cell

electrode. In addition, the energy density and power density were calculated using Eqs. (5) and (6) [64, 65]:

$$E = \frac{I \int V dt}{M3.6}, \quad (5)$$

$$P = E/\Delta t, \quad (6)$$

where E (Wh kg⁻¹) is the energy density, I (A) is the applied current, $\int V dt$ is the galvanostatic discharge current area, M (g) is the active mass, P (W kg⁻¹) is the power density, and Δt (s) is the discharge time. Figure 7d presents the Ragone plot of the fabricated ASC devices. The PAN@NiCu(CO₃)(OH)₂ electrode ASC shows that the highest energy density with 90 W h kg⁻¹ at a power density of 835 W kg⁻¹ and current density of 2 A g⁻¹. As the current density changes to 15 A g⁻¹, the energy density decreases to 36 W h kg⁻¹ at a power density of 9268 W kg⁻¹. The PAN@NiCu(CO₃)(OH)₂ electrode achieved better energy and power densities than that of the Ni-foam@NiCu(CO₃)(OH)₂ electrode ACS, NiO//carbon [66], Ni(OH)₂//carbon [67], and MnO₂//carbon [68]. These results can aid the development of flexible and wearable faradaic capacitors with enhanced electrochemical performance by synthesizing PAN nanomeshes and modifying their surface through the growth of binary metal hydroxy-carbonates. Thus, PAN@NiCu(CO₃)(OH)₂ nanowires are promising materials of the positive electrode for high-performance supercapacitors.

Conclusions

Faradaic capacitors require a large specific surface area for redox reactions. To provide this large surface area, mesoporous NiCu(CO₃)(OH)₂ composites were grown on PAN nanofiber substrates using a hydrothermal method. PAN nanofibers were fabricated via the electrospinning method, giving a substrate with a nano-sized diameter and high specific surface area. Thus, the beneficial properties of high-performance SCs can arise from the structure as well as the material. The composite of NiCu(CO₃)(OH)₂ on PAN nanofibers provided a highly porous structure and a large surface area, which significantly improved the electrolyte penetration and electrical conductivity of the active materials, while providing a convenient electron diffusion path. The optimized PAN@NiCu(CO₃)(OH)₂ electrode showed an excellent maximum specific capacity of 870 mAh g⁻¹ at 3 A g⁻¹ and superior cycling stability with capacitance retention of 84.1% after 5000 cycles. An asymmetric supercapacitor was fabricated using the PAN@NiCu(CO₃)(OH)₂ composite as the cathode and commercial graphene as the anode. The ASC delivered a high energy density of 90 W h kg⁻¹ at a power density of 835 W kg⁻¹ at 2 A g⁻¹ and maintained 36 W h kg⁻¹ at a high power density of 9268 W kg⁻¹ at 15 A g⁻¹ with satisfactory cycling stability, retaining 90.1% of its capacitance after 5000

cycles. On the other hand, the previously studied NiCu(CO₃)(OH)₂//graphene ASC of Ni-foam substrate showed a relatively low energy density value with the energy density of 27 W h kg⁻¹ at 2 A g⁻¹. These results suggest that the optimized unique NiCu(CO₃)(OH)₂ composite on the PAN nanofiber substrate electrode is a potential material for use in wearable devices demanding flexibility. In conclusion, polymer and transition metal composite electrodes will potentially lead to further research and development of electrode industrialization and high-performance supercapacitors.

Experiment

Materials

The materials used in this study were Ni foam (110 PPI pore density, 320 g m⁻² mass density), polyacrylonitrile (PAN), dimethylformamide (DMF), nickel nitrate hexahydrate (Ni(NO₃)₂·6H₂O), copper nitrate trihydrate (Cu(NO₃)₂·3H₂O), CO(NH₂)₂ (urea), and KOH (potassium hydroxide). All chemical reagents were used without further purification.

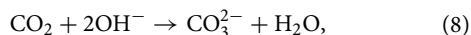
Electrode preparation

Ni foam as substrate: Two pieces of Ni foam (2 × 4 cm) were cleaned for 10 min by rinsing with 2.0 mol L⁻¹ of HCl, washing with DI water and ethanol for 10 min each, and then drying at 50 °C in an oven for 12 h.

PAN nanofibers as substrates: PAN nanofibers were fabricated using the electrospinning method. The experimental conditions were set to PAN (0.72 g) and DMF (9 mL). As demonstrated in our previous experiments, this condition allows for the creation of an optimal nanofiber material. The applied voltage was approximately 15 kV, and the current was adjusted to a constant value. The PAN solution was poured into a syringe attached to a capillary tip with a 0.5 mm diameter, and the flow rate was uniform (20 mL h⁻¹). The capillary tip and deposition position were kept constant at 15 cm. The substrate for PAN was not used separately, and the fabricated PAN nanofibers were directly used as the electrode substrate.

Fabrication of the Ni–Cu electrode: Optimized quantities of 6 mmol of Ni, 3 mmol of Cu, and 13 mmol of urea were placed in 50 mL of DI water and this solution was stirred for 10 min. This solution was moved to a 50 mL autoclave vessel. The Ni foam and PAN-nanofiber substrates were immersed in the aqueous solution separately and heated at 160 °C for 12 h via the hydrothermal method to synthesize NiCu(CO₃)(OH)₂. To remove surface impurities, the electrodes were washed several times with DI water and ethanol. And then, to remove adsorbed solvents, the samples were dried at 50 °C for 12 h. In the synthesis, urea is the source of both carbonate and hydroxyl anions, as

indicated in Eqs. (7–9). The synthesis of $\text{NiCu}(\text{CO}_3)(\text{OH})_2$ is as follows (7–9) [10, 27].



Material characterization

The phases of the samples were characterized using X-ray diffraction (XRD; STOE STADI MP), which were measured over a range of 5–60° (2θ). X-ray photoelectron spectroscopy (XPS; ESCALAB250, VG Scientifics) was examined to analyze the valence states of the $\text{NiCu}(\text{CO}_3)(\text{OH})_2$ composite powder. The morphology analysis of the $\text{PAN@NiCu}(\text{CO}_3)(\text{OH})_2$ nanowire electrodes was performed through scanning electron microscopy (SEM; FEI Strata Dual Beam 235). Transmission electron microscopy was measured using (TEM; JEOL JEM-2200 FS) with energy-dispersive X-ray spectroscopy.

Electrochemical measurements

All electrochemical tests were performed on an electrochemical workstation (VersaSTAT, Princeton Applied Research) using a three-electrode configuration using a 1 M KOH aqueous solution as the electrolyte at room temperature. $\text{NiCu}(\text{CO}_3)(\text{OH})_2$ nanowire composites on PAN nanofibers were directly used as the cathode electrode, and Pt and Hg/HgO were used as the counter and reference electrodes, respectively. The cyclic voltammetry (CV) curves were plotted in a potential range between 0.15 and 0.6 V at different scan rates from 5 to 50 mV s^{-1} . The galvanostatic charge–discharge (GCD) processes were evaluated by cycling the potential from 0 to 0.45 V at current densities of 3, 4, 5, 8, 10, and 15 A g^{-1} .

Acknowledgments

This study was supported by the Global Frontier Hybrid Interface Materials (GFHIM) program of the National Research Foundation of Korea (NRF) funded by the Ministry of Science, ICT & Future Planning (2013M3A6B1078874). The authors are thankful to the University of Cologne for infrastructural support and for hosting Dr. Damin Lee.

Declarations

Conflicts of interest There are no conflicts of interest to declare.

Open Access

This article is licensed under a Creative Commons Attribution 4.0 International License, which permits use, sharing, adaptation, distribution and reproduction in any medium or format, as long as you give appropriate credit to the original author(s) and the source, provide a link to the Creative Commons licence, and indicate if changes were made. The images or other third party material in this article are included in the article's Creative Commons licence, unless indicated otherwise in a credit line to the material. If material is not included in the article's Creative Commons licence and your intended use is not permitted by statutory regulation or exceeds the permitted use, you will need to obtain permission directly from the copyright holder. To view a copy of this licence, visit <http://creativecommons.org/licenses/by/4.0/>.

References

1. P. Kumar, K.-H. Kim, V. Bansal, P. Kumar, Nanostructured materials: A progressive assessment and future direction for energy device applications. *Coordin. Chem. Rev.* **353**, 113 (2017)
2. L.B. Huang, W. Xu, J. Hao, Energy device applications of synthesized 1D polymer nanomaterials. *Small* **13**, 1701820 (2017)
3. P. Dong, M.-T.F. Rodrigues, J. Zhang, R.S. Borges, K. Kalaga, A.L. Reddy, G.G. Silva, P.M. Ajayan, J. Lou, A flexible solar cell/supercapacitor integrated energy device. *Nano Energy* **42**, 181 (2017)
4. H. Li, Z. Tang, Z. Liu, C. Zhi, Evaluating flexibility and wearability of flexible energy storage devices. *Joule* **3**, 613 (2019)
5. J. Wang, X. Zhang, Z. Li, Y. Ma, L. Ma, Recent progress of biomass-derived carbon materials for supercapacitors. *J. Power Sources* **451**, 227794 (2020)
6. R. Liu, A. Zhou, X. Zhang, J. Mu, H. Che, Y. Wang, T. Wang, Z. Zhang, Z. Kou, Fundamentals, advances and challenges of transition metal compounds-based supercapacitors. *Chem. Eng. J.* **412**, 128611 (2021)
7. T.-F. Yi, H. Chang, T.-T. Wei, S.-Y. Qi, Y. Li, Y.-R. Zhu, Approaching high-performance electrode materials of ZnCo_2S_4 nanoparticle wrapped carbon nanotubes for supercapacitors. *J. Materiomics* **7**, 563 (2021)
8. S. Biswas, V. Sharma, T. Singh, A. Chandra, External vibrations can destroy the specific capacitance of supercapacitors—from experimental proof to theoretical explanations. *J. Mater. Chem. A* **9**, 6460 (2021)

9. S.I. Wong, H. Lin, J. Sunarso, B.T. Wong, B. Jia, Optimization of ionic-liquid based electrolyte concentration for high-energy density graphene supercapacitors. *Appl. Mater. Today* **18**, 100522 (2020)
10. D. Lee, H.W. Lee, N.M. Shinde, J.M. Yun, S. Mathur, K.H. Kim, Synthesis of nickel-copper composite with controllable nanostructure through facile solvent control as positive electrode for high-performance supercapacitors. *Dalton Trans* **49**, 13123 (2020)
11. T. Wang, M. Liu, H. Ma, Facile synthesis of flower-like copper-cobalt sulfide as binder-free faradaic electrodes for supercapacitors with improved electrochemical properties. *Nanomaterials* **7**, 140 (2017)
12. Y. Li, Z. Kang, X. Yan, S. Cao, M. Li, Y. Guo, Y. Huan, X. Wen, Y. Zhang, A three-dimensional reticulate CNT-aerogel for a high mechanical flexibility fiber supercapacitor. *Nanoscale* **10**, 9360 (2018)
13. X. Zhang, X. Liu, Y. Zeng, Y. Tong, X. Lu, Oxygen defects in promoting the electrochemical performance of metal oxides for supercapacitors: Recent advances and challenges. *Small Methods* **4**, 1900823 (2020)
14. J. Chen, J. Xu, S. Zhou, N. Zhao, C.-P. Wong, Amorphous nanostructured FeOOH and Co-Ni double hydroxides for high-performance aqueous asymmetric supercapacitors. *Nano Energy* **21**, 145 (2016)
15. V.S. Kumbhar, H. Lee, J. Lee, N.R. Chodankar, K. Lee, Mesoporous design of ultrathin NiO nanosheet-coated vertically aligned hexagonal CoS nanoplate core-shell array for flexible all-solid-state supercapacitors. *J. Alloys Compd.* **863**, 158064 (2021)
16. Y. Zhao, Y. Zhang, Y. Cheng, W. Zhao, W. Chen, C. Meng, C. Huang, Synthesis of $\text{Co}_2\text{SiO}_4/\text{Ni}(\text{OH})_2$ core-shell structure as the supercapacitor electrode material with enhanced electrochemical properties. *Mater. Lett.* **282**, 128774 (2021)
17. K. Karuppasamy, D. Vikraman, J.-H. Jeon, S. Ramesh, H.M. Yadav, V.R. Jothi, R. Bose, H.S. Kim, A. Alfantazi, H.-S. Kim, Highly porous, hierarchical microglobules of Co_3O_4 embedded N-doped carbon matrix for high performance asymmetric supercapacitors. *Appl. Surf. Sci.* **529**, 147147 (2020)
18. Z. Song, W. Liu, Q. Zhou, L. Zhang, Z. Zhang, H. Liu, J. Du, J. Chen, G. Liu, Z. Zhao, Cobalt hexacyanoferrate/ MnO_2 nanocomposite for asymmetrical supercapacitors with enhanced electrochemical performance and its charge storage mechanism. *J. Power Sources* **465**, 228266 (2020)
19. M. Chamakh, A.I. Ayes, Production and investigation of flexible nanofibers of sPEEK/PVP loaded with RuO_2 nanoparticles. *Mater. Design* **204**, 109678 (2021)
20. S. Vijayakumar, S. Nagamuthu, G. Muralidharan, Supercapacitor studies on NiO nanoflakes synthesized through a microwave route. *ACS appl. Mater. inter* **5**, 2188 (2013)
21. W. Lv, L. Li, Q. Meng, X. Zhang, Molybdenum-doped CuO nanosheets on Ni foams with extraordinary specific capacitance for advanced hybrid supercapacitors. *J. Mater. Sci.* **55**, 2492 (2020)
22. V.T. Chebrolu, B. Balakrishnan, V. Raman, I. Cho, J.-S. Bak, K. Prabakar, H.-J. Kim, Co-electrodeposition of $\text{NiCu}(\text{OH})_2/\text{Ni-Cu-Se}$ hierarchical nanoparticle structure for supercapacitor application with enhanced performance. *Appl. Surf. Sci.* **506**, 145015 (2020)
23. D. Lee, Q.X. Xia, R.S. Mane, J.M. Yun, K.H. Kim, Direct successive ionic layer adsorption and reaction (SILAR) synthesis of nickel and cobalt hydroxide composites for supercapacitor applications. *J. Alloys. Compd* **722**, 809 (2017)
24. S. Liu, K. Hui, K. Hui, V.V. Jadhav, Q.X. Xia, J.M. Yun, Y. Cho, R.S. Mane, K.H. Kim, Facile synthesis of microsphere copper cobalt carbonate hydroxides electrode for asymmetric supercapacitor. *Electrochim. Acta* **188**, 898 (2016)
25. T.M. Masikhwa, J.K. Dangbegnon, A. Bello, M.J. Madito, D. Momodu, N. Manyala, Preparation and electrochemical investigation of the cobalt hydroxide carbonate/activated carbon nanocomposite for supercapacitor applications. *J. Phys. Chem. Solids* **88**, 60 (2016)
26. D. Lee, Q.X. Xia, J.M. Yun, K.H. Kim, High-performance cobalt carbonate hydroxide nano-dot/ $\text{NiCo}(\text{CO}_3)(\text{OH})_2$ electrode for asymmetric supercapacitors. *Appl. Surf. Sci.* **433**, 16 (2018)
27. M. Azad, Z. Hussain, M.M. Baig, MWCNTs/ NiS_2 decorated Ni foam based electrode for high-performance supercapacitors. *Electrochim. Acta* **345**, 136196 (2020)
28. M. Huang, F. Li, J.Y. Ji, Y.X. Zhang, X.L. Zhao, X. Gao, Facile synthesis of single-crystalline NiO nanosheet arrays on Ni foam for high-performance supercapacitors. *CrystEngComm* **16**, 2878 (2014)
29. D. Lee, J.M. Yun, K.H. Kim, Preparation and electrochemical properties of nickel iron carbonate hydroxide as a cathode electrode material for asymmetric supercapacitors. *Nanosci. Nanotech. Lett.* **10**, 741 (2018)
30. M. Panapoy, A. Dankeaw, B. Ksapabutr, Electrical conductivity of PAN-based carbon nanofibers prepared by electrospinning method. *Thammasat Int J. Sc. Tech.* **13**, 11 (2008)
31. C. Hellert, J.L. Storck, T. Grothe, B. Kaltschmidt, A. Hütten, A. Ehrmann: Positioning and aligning electrospun PAN fibers by conductive and dielectric substrate patterns, in: *Macromolecular Symposia, Macromol. Symposia*, 395, 2000213 (2021).
32. S. Temesgen, M. Rennert, T. Tesfaye, M. Nase, Review on spinning of biopolymer fibers from starch. *Polymers* **13**, 1121 (2021)
33. E. Boyraz, F. Yalcinkaya, Hydrophilic surface-modified PAN nanofibrous membranes for efficient oil-water emulsion separation. *Polymers* **13**, 197 (2021)

34. T. Yang, H. Yang, S.J. Zhen, C.Z. Huang, Hydrogen-bond-mediated in situ fabrication of AgNPs/Agar/PAN electrospun nanofibers as reproducible SERS substrates. *ACS Appl. Mater. Inter.* **7**, 1586 (2015)
35. M. Gao, L. Zeng, J. Nie, G. Ma, Polymer-metal-organic framework core-shell framework nanofibers via electrospinning and their gas adsorption activities. *RSC Adv* **6**, 7078 (2016)
36. D. Potphode, M.S. Sayed, T.L. Tamang, J.-J. Shim, High-performance binder-free flower-like $(\text{Ni}_{0.66}\text{Co}_{0.3}\text{Mn}_{0.04})_2(\text{OH})_2(\text{CO}_3)$ array synthesized using ascorbic acid for supercapacitor applications. *Chem. Eng. J* **378**, 122129 (2019)
37. G. Zhang, P. Qin, R. Nasser, S. Li, P. Chen, J. Song, Synthesis of $\text{Co}(\text{CO}_3)_{0.5}(\text{OH})/\text{Ni}_2(\text{CO}_3)(\text{OH})_2$ nanobelts and their application in flexible all-solid-state asymmetric supercapacitor. *Chem. Eng. J* **387**, 124029 (2020)
38. G. Yilmaz, C.F. Tan, Y.F. Lim, G.W. Ho, Pseudomorphic transformation of interpenetrated prussian blue analogs into defective nickel iron selenides for enhanced electrochemical and photoelectrochemical water splitting. *Adv. Energy Mater.* **9**, 1802983 (2019)
39. S. Ding, T. Zhu, J.S. Chen, Z. Wang, C. Yuan, X.W.D. Lou, Controlled synthesis of hierarchical NiO nanosheet hollow spheres with enhanced supercapacitive performance. *J. Mater. Chem.* **21**, 6602 (2011)
40. A. Mansour, Characterization of $\beta\text{-Ni}(\text{OH})_2$ by XPS. *Surf. Sci. Spectra* **3**, 239 (1994)
41. N. Pauly, S. Tougaard, F. Yubero, Determination of the Cu 2p primary excitation spectra for Cu, Cu_2O and CuO. *Surf. Sci.* **620**, 17 (2014)
42. R. Morent, N. De Geyter, C. Leys, L. Gengembre, E. Payen, Comparison between XPS-and FTIR-analysis of plasma-treated polypropylene film surfaces, *Surface and Interface Analysis: An International Journal devoted to the development and application of techniques for the analysis of surfaces. Interfaces. Thin Films* **40**, 597 (2008)
43. L. Fen-rong, L. Wen, G. Hui-qing, L. Bao-qing, B. Zong-qing, H. Rui-sheng, XPS study on the change of carbon-containing groups and sulfur transformation on coal surface. *J. Fuel Chem. Technol.* **39**, 81 (2011)
44. D. Lee, N. Shinde, J.C. Ding, J. Fu, R.K. Sahoo, H.W. Lee, J.M. Yun, H.-C. Shin, K.H. Kim, Improvement of electrical performance by surface structure of Ni-material as a high-performance asymmetric supercapacitor electrode. *Ceram. Inter.* **46**, 11189 (2020)
45. Q. Zhou, J. Huang, C. Li, Z. Lv, H. Zhu, G. Hu, Wrapping CuCo_2S_4 arrays on nickel foam with $\text{Ni}_2(\text{CO}_3)(\text{OH})_2$ nanosheets as a high-performance faradaic electrode. *New J. Chem.* **43**, 5904 (2019)
46. H. Yang, Effects of supercapacitor physics on its charge capacity. *IEEE Trans. Power Electr.* **34**, 646 (2018)
47. A.M. Patil, X. Yue, A. Yoshida, S. Li, X. Hao, A. Abudula, G. Guan, Redox-ambitious route to boost energy and capacity retention of pouch type asymmetric solid-state supercapacitor fabricated with graphene oxide-based battery-type electrodes. *Appl. Mater. Today* **19**, 100563 (2020)
48. J. Yan, Z. Fan, W. Sun, G. Ning, T. Wei, Q. Zhang, R. Zhang, L. Zhi, F. Wei, Advanced asymmetric supercapacitors based on $\text{Ni}(\text{OH})_2/\text{graphene}$ and porous graphene electrodes with high energy density. *Adv. Funct. Mater* **22**, 2632 (2012)
49. Y. Wang, B. Chang, D. Guan, K. Pei, Z. Chen, M. Yang, X. Dong, Preparation of nanospherical porous NiO by a hard template route and its supercapacitor application. *Mater. Lett.* **135**, 172 (2014)
50. C. Wang, J. Xu, M.F. Yuen, J. Zhang, Y. Li, X. Chen, W. Zhang, Hierarchical composite electrodes of nickel oxide nanoflake 3D graphene for high-performance pseudocapacitors. *Adv. Funct. Mater.* **24**, 6372 (2014)
51. G.S. Gund, D.P. Dubal, S.S. Shinde, C.D. Lokhande, Architected morphologies of chemically prepared NiO/MWCNTs nanohybrid thin films for high performance supercapacitors. *ACS Appl. Mater. Inter.* **6**, 3176 (2014)
52. Z. Li, M. Shao, L. Zhou, R. Zhang, C. Zhang, J. Han, M. Wei, D.G. Evans, X. Duan, A flexible all-solid-state micro-supercapacitor based on hierarchical $\text{CuO}@$ layered double hydroxide core-shell nanoarrays. *Nano Energy* **20**, 294 (2016)
53. K. Krishnamoorthy, S.-J. Kim, Growth: Characterization and electrochemical properties of hierarchical CuO nanostructures for supercapacitor applications. *Mater. Res. Bull.* **48**, 3136 (2013)
54. M.B. Gholivand, H. Heydari, A. Abdolmaleki, H. Hosseini, Nanostructured CuO/PANI composite as supercapacitor electrode material. *Mater. Sci. Semicon. Proc.* **30**, 157 (2015)
55. S. Shinde, H. Yadav, G. Ghodake, A. Kadam, V. Kumbhar, J. Yang, K. Hwang, A. Jagadale, S. Kumar, D. Kim, Using chemical bath deposition to create nanosheet-like CuO electrodes for supercapacitor applications. *Colloid Surf. B* **181**, 1004 (2019)
56. Y. Wang, C. Shen, L. Niu, R. Li, H. Guo, Y. Shi, C. Li, X. Liu, Y. Gong, Hydrothermal synthesis of $\text{CuCo}_2\text{O}_4/\text{CuO}$ nanowire arrays and RGO/ Fe_2O_3 composites for high-performance aqueous asymmetric supercapacitors. *J. Mater. Chem. A* **4**, 9977 (2016)
57. Y. Feng, W. Liu, Y. Wang, W. Gao, J. Li, K. Liu, X. Wang, J. Jiang, Oxygen vacancies enhance supercapacitive performance of CuCo_2O_4 in high-energy-density asymmetric supercapacitors. *J. Power Sources* **458**, 228005 (2020)
58. S.M. Pawar, B.S. Pawar, P.T. Babar, A.T.A. Ahmed, H.S. Chavan, Y. Jo, S. Cho, J. Kim, B. Hou, A.I. Inamdar, Nanoporous CuCo_2O_4 nanosheets as a highly efficient bifunctional electrode for

- supercapacitors and water oxidation catalysis. *Appl. Surf. Sci* **470**, 360 (2019)
59. L. Abbasi, M. Arvand, Engineering hierarchical ultrathin CuCo_2O_4 nanosheets array on Ni foam by rapid electrodeposition method toward high-performance binder-free supercapacitors. *Appl. Surf. Sci* **445**, 272 (2018)
 60. A. Bera, A. Maitra, A.K. Das, L. Halder, S. Paria, S.K. Si, A. De, S. Ojha, B.B. Khatua, A quasi-solid-state asymmetric supercapacitor device based on honeycomb-like nickel-copper-carbonate-hydroxide as a positive and iron oxide as a negative electrode with superior electrochemical performances. *ACS Appl. Electron. Mater* **2**, 177 (2020)
 61. Q. Zhou, T. Wei, Z. Liu, L. Zhang, B. Yuan, Z. Fan, Nickel hexacyanoferrate on graphene sheets for high-performance asymmetric supercapacitors in neutral aqueous electrolyte. *Electrochim. Acta* **303**, 40 (2019)
 62. L. Zhang, H. Gong, Unravelling the correlation between nickel to copper ratio of binary oxides and their superior supercapacitor performance. *Electrochim. Acta* **234**, 82 (2017)
 63. S. Song, L. Zhang, H. Shi, Facile synthesis of three-dimensional nanostructured $\text{Ni}(\text{HCO}_3)_2/(\text{Cu}_{0.2}\text{Ni}_{0.8})\text{O}$ as high-performance pseudo-capacitance electrode. *J. Alloy. Compd* **763**, 791 (2018)
 64. S. Kumar, G. Saeed, L. Zhu, K.N. Hui, N.H. Kim, J.H. Lee, 0D to 3D carbon-based networks combined with pseudocapacitive electrode material for high energy density supercapacitor: A review. *Chem. Eng. J* **403**, 126352 (2020)
 65. H.-G. Jung, N. Venugopal, B. Scrosati, Y.-K. Sun, A high energy and power density hybrid supercapacitor based on an advanced carbon-coated $\text{Li}_4\text{Ti}_5\text{O}_{12}$ electrode. *J. Power Sources* **221**, 266 (2013)
 66. Q. Qu, P. Zhang, B. Wang, Y. Chen, S. Tian, Y. Wu, R. Holze, Electrochemical performance of MnO_2 nanorods in neutral aqueous electrolytes as a cathode for asymmetric supercapacitors. *J. Phys. Chem. C* **113**, 14020 (2009)
 67. Y.-H. Lee, K.-H. Chang, C.-C. Hu, Differentiate the pseudo-capacitance and double-layer capacitance contributions for nitrogen-doped reduced graphene oxide in acidic and alkaline electrolytes. *J. Power Sources* **227**, 300 (2013)
 68. J. Huang, P. Xu, D. Cao, X. Zhou, S. Yang, Y. Li, G. Wang, Asymmetric supercapacitors based on $\beta\text{-Ni}(\text{OH})_2$ nanosheets and activated carbon with high energy density. *J. Power Sources* **246**, 371 (2014)